This article has been accepted for publication in a future issue of this journal, but has not been fully edited. Content may change prior to final publication. Citation information: DOI 10.1109/TIP.2020.2973810, IEEE Transactions on Image Processing

Simultaneous Surface Reflectance and Fluorescence Spectra Estimation

Henryk Blasinski, Joyce Farrell and Brian Wandell

Abstract—**There is widespread interest in estimating the fluorescence properties of natural materials in an image. However, the separation between reflected and fluoresced components is difficult, because it is impossible to distinguish reflected and fluoresced photons without controlling the illuminant spectrum. We show how to jointly estimate the reflectance and fluorescence from a single set of images acquired under multiple illuminants. We present a framework based on a linear approximation to the physical equations describing image formation in terms of surface spectral reflectance and fluorescence due to multiple fluorophores. We relax the non-convex, inverse estimation problem in order to jointly estimate the reflectance and fluorescence properties in a single optimization step. We provide a software implementation of the solver for our method and prior methods. We evaluate the accuracy and reliability of the method using both simulations and experimental data. To evaluate the methods experimentally we built a custom imaging system using a monochrome camera, a filter wheel with bandpass transmissive filters and a small number of light emitting diodes. We compared the methods based upon our framework with the ground truth as well as with prior methods.**

Index Terms—**Reflectance and Fluorescence Spectra Recovery, Multispectral and Hyperspectral Imaging, Image Color Analysis, Inverse Problems**

I. INTRODUCTION

MATERIALS are commonly characterized by their surface reflectance spectra, which describe the fraction of incident photons that are reflected at each wavelength. In addition to reflectance, some materials absorb light in some wavelengths and then emit photons at longer wavelengths, a phenomenon called fluorescence. Fluorescent materials are common in nature [25], [42], man-made objects such as paper, textiles, displays [15], [19], [37], or biological tissues [12], [26], [28]. In addition, the discovery of fluorophores that selectively bind to specific molecules has been extremely useful in biological and medical sciences [5], [24].

To better characterize materials, it is useful to separate fluoresced photons from reflected ones, and there is widespread interest in natural and biological imaging methods that simultaneously estimate and disambiguate reflected and fluoresced photons [9], [11], [21], [35], [39], [46], [48]. In this paper we describe an algorithm for simultaneously estimating reflectance and fluorescence. We design, implement, and evaluate a simple experimental system that performs this separation.

For the purpose of putting our work in context, it is useful to divide reflectance-fluorescence estimation algorithms (Table I) into two categories. We use the term *bispectral separation* to describe methods that use illumination and surface radiance spectra at densely sampled measurements in the wavelength domain. The approach combines complex instrumentation with relatively simple reconstruction algorithms. For example, Fuchs [11] described a method that measures the sample radiance under ambient light with and without an additional, fluorescence exciting illuminant. The fluorescence term is estimated by comparing the radiance ratios for wavelengths longer than the emission peak. A similar approach was presented by Tominaga *et al.* [38], [39], [40] who performed spectral separation using multispectral images of a scene acquired under two different, broadband light sources. These ideas were further extended by Fu *et al.* [9] who used a multispectral camera together with light patterns with spectral power distributions sinusoidally modulated in the wavelength domain. They compared radiances for two illuminants that were phase-shifted in the wavelength domain. This approach requires multispectral acquisition and a spectrally controlled light source. A simpler method, requiring only a hyperspectral imager, was developed by Zheng *et al.* [48] who proposed a compact, four parameter fluorescent spectra parameterization based on Cauchy distribution and an estimation algorithm that solves a sequence of optimizations. Zheng *et al.* [47] also use a single hyperspectral capture under illuminant with spectrally uneven distribution to estimate reflectance and emission spectra only.

Computational separation methods couple simpler instrumentation and fewer measurements with more complex algorithms that incorporate knowledge about the likely properties of the signals. Several algorithms use compressive sensing ideas and coarsely sampled measurements in the wavelength domain. For example, Zhang [46] use three-band (RGB) images to distinguish between reflected and fluoresced photons. Their Independent Component Analysis (ICA) based algorithm uses two images acquired under different illuminants and assumes a camera spectral responsivity model of Dirac delta functions in the wavelength domain. Lam and Sato [21] and Fu *et al.* [8], [10], extend this work to estimate reflectance and fluorescence spectra. Lam and Sato first estimate the reflectance component at about ten different wavelengths and then derive fluorescence components by subtracting the estimated reflectance contribution from the measurements. Fu *et al.* [8], [10] acquire a sequence of RGB images under nine different, narrowband illuminants. They develop a multi-step algorithm that estimates the chromaticity coordinates of the reflectance and fluorescence spectra and then searches a fluorophore database to determine the likely emission spectrum. Finally, Suo *et al.* [35] estimate the reflectance spectrum and

All authors are with the Department of Electrical Engineering, Stanford University, CA 94305. E-mail: {hblasins, jefarrell, wandell}@stanford.edu

TABLE I: Comparison between existing reflectance and fluorescence estimation and separation algorithms. The 'Camera' column describes the number of transmissive filters of the imaging system. Similarly 'Lights' provide the number (#) of illuminants and whether those were narrowband (NB) or broadband (BB). Finally the algorithm can provide an estimate of the reflectance (R), one or more fluorophores (F), and these can be characterized spectrally (Spect.) or in terms of intensity (Int.).

Class	Author	Camera (# bands)	Lights			Method	Estimate			
			#	NB	BB		R	F	Spect.	Int.
Bispectral	Tominaga *et al.* [39]	~ 30	2		✓	Within-band ratios	✓	1	✓	
	Fu *et al.* [9]	~ 30	2	✓		Within-band ratios	✓	1	✓	
	Zheng *et al.* [48]	~ 30	3		✓	Sequence of optimizations	✓	1	✓	
	Lam *et al.* [21]	~ 30	~ 10	✓		Multistep estimation	✓	1	✓	
	Zheng *et al.* [47]	57	1		✓	Single Optimization	✓	1	✓	
Comput.	Zhang *et al.* [46]	3	2		✓	Ind. Component Analysis		1		✓
	Suo *et al.* [35]	~ 10	~ 6	✓		Biconvex optimization	✓	1+		✓
	Fu *et al.* [8], [10]	3	~ 11	✓		Sequence of optimizations	✓	1	✓	
	Proposed	~ 7	~ 15	✓		Single Optimization	✓	1+	✓	

the Donaldson matrix, describing fluorescence properties of a surface, through nuclear norm minimization using Alternating Direction Minimization (ADM).

We present a collection of computational separation methods to simultaneously estimate the reflectance, excitation and emission spectra of a surface. Our approach uses simplified hardware and acquisition steps, and leverages computation and modelling to obtain spectral estimates. This framework builds on, and unifies several prior approaches [8], [10], [35], [48]. The methods also extend the active illumination reflection estimation methods [29], [30], and the general case of fluorescence unmixing methods when surface spectral properties are unknown [1], [17]. We formulate the reflectance and fluorescence spectra estimation as an inverse estimation problem, which we jointly solve in a single step for all unknown quantities, avoiding the pitfalls of sequential estimation [10]. Our estimates are full spectral power distributions rather than estimates of reflected and fluoresced radiance contributions in a particular camera channel [35], [46]. We improve on prior approaches by reducing the number of assumptions about the fluorescent signal, specifically we do not assume chromaticity invariance. Consequently our algorithms can be used to estimate fluorescent properties of mixtures of different fluorophores, which in general violate this assumption. We also do not require prior knowledge of the number of fluorophores present in the sample [35]. Our methods assume that the fluorescent materials exhibit the typical Stokes Shift, *i.e.* their peak emission wavelength is longer than their peak absorption wavelength; but, with some modifications the methods are equally applicable to anti-Stokes materials.

There are many situations where it may be necessary to resolve fluorescent signals from multiple fluorophores. In some cases the imaging targets inherently contain mixtures of fluorophores. For example, coral reefs are known to contain multiple fluorophores, and it is useful to separate them in order to assess their health [41], [45]. There is a very large literature on the use of multiple endogenous fluorophores in biological tissue for assessing tissue health [26]. In other cases, physical limitations of the optics and pixel spacing can cause signals from distinct spatial locations to combine in a single pixel, which measures multiple substrates. This phenomenon can occur across all types of imaging systems. One example is remote sensing where a satellite pixel measures a region of the sea that includes more than one type of coral reef. Another example is microscopy, where cells with different fluorophores may be interleaved within the tissue. Hence, a single pixel within the digital microscope picks up the superposition of fluorescent signals from multiple cell types. To illustrate this case consider fluorescein angiography of the retina. In this case the blood vessels on the inner retina surface contain one type of fluorescence, the cells within the retina are inherently auto-fluorescent, and the light is also reflected from the pigment epithelium layer [14], [33]. Although the fluorescent components are confined to distinct substrates, the image pixels contain an optically mixed signal.

We recognize that there are use cases in which a sample contains a single fluorophore. We demonstrate that such scenarios can be treated as a special case of our general algorithm. By explicitly limiting the solution space to a single fluorophore, the algorithms can be simplified and accelerated leading to more computationally efficient separation methods. Furthermore, whenever estimating the fluorescent excitation spectrum is not necessary, the algorithms can be further simplified by solving for the reflectance and fluorescence emission only.

The algorithms can be applied to data collected from a wide variety of imaging systems, including different types of sensors and light sources. The choice of sensor channels and light sources will influence the algorithm performance. We use a simulation environment to help designers optimize system design given a specific choice of fluorophores.

To evaluate the algorithms, we built a system, composed of off-the-shelf light emitting diodes (LED), transmissive filters and a monochrome camera. A target scene is illuminated with a single narrowband light source, from a small collection of available lights, and images of this scene are captured through a few narrowband filters. From the calibrated system characteristics, such as filter transmissivities or illuminant spectral power distributions, we estimate how accurately the algorithm reconstructs and separates reflected and fluoresced photons.

Section II describes the image formation model for fluorescent surfaces. Section III presents the optimization framework

This article has been accepted for publication in a future issue of this journal, but has not been fully edited. Content may change prior to final publication. Citation information: DOI 10.1109/TIP.2020.2973810, IEEE Transactions on Image Processing

and formulates spectral estimation and separation between reflectance and fluorescence radiance components as an inverse estimation problem. We analyze the limitations of the algorithms (Section IV) and present the hardware system with experimental evaluations (Section V). We then discuss the experimental results (Section VI) and present our conclusions (Section VII). The source code and experimental results we present in the major figures are all accessible online.

II. FLUORESCENT IMAGE FORMATION MODEL

Digital camera pixel response level m is linearly related to the scene radiance ρ [7]

$$m = g \int q_e(\lambda)s(\lambda)\rho(\lambda)d\lambda, \tag{1}$$

where q_e the photodetector quantum efficiency and s is the color filter transmissivity. The scalar g combines a collection of camera parameters including the sensor gain, exposure duration and the aperture size. For any particular camera this combination of parameters in g and the color filters s can be fixed and calibrated.

The radiance, ρ, of any point in the scene is a superposition of radiances due to reflected ρ_r, and fluoresced light, ρ_f. Let $\rho(\lambda)$ denote the total radiance at some wavelength λ, then

$$\rho(\lambda) = \rho_r(\lambda) + \rho_f(\lambda), \tag{2}$$

Assuming smooth and isotropic Lambertian surfaces, the reflected radiance at some wavelength λ can be computed as a product of the illuminant $l(\lambda)$ and the surface reflectance $r(\lambda)$

$$\rho_r(\lambda) = l(\lambda)r(\lambda). \tag{3}$$

Fluorescent radiance can be produced by a number of different fluorescent compounds present in the sample. Typically their individual contributions $e_{f,z}(\lambda)$ are additive [1], [20]

$$\rho_f(\lambda) = \sum_{z=1}^{Z} \rho_{f,z}(\lambda), \tag{4}$$

where z indexes over different fluorophores.

In the most general case the fluorescent radiance due to a single fluorophore $\rho_{f,z}(\lambda)$ is described by a two dimensional function $e_{xm,z}(\lambda, \lambda_x)$ [44]. This function expresses the number of emitted photons at a particular wavelength λ as a fraction of incident monochromatic light of some other and different wavelength λ_x. If a broadband light source is used it is necessary to consider fluorescence emissions arising from illumination at all spectral bands of the incident light

$$\rho_{f,z}(\lambda) = \int e_{xm,z}(\lambda, \lambda_x)l(\lambda_x)d\lambda_x. \tag{5}$$

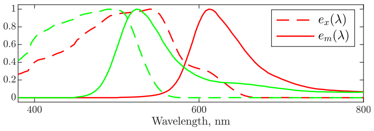

(a) Fluorophores

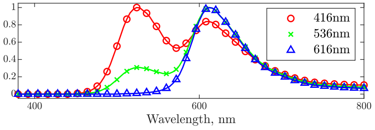

(b) Emitted lights

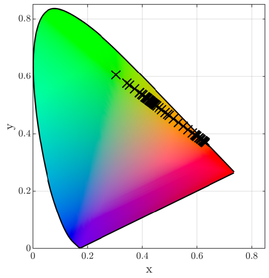

(c) Chromaticity

Fig. 1: Chromaticity invariance of the fluoresced signal is violated when the sample includes two or more fluorophores. (a) The excitation (dashed) and emission (solid) spectra of two fluorophores (green and blue). (b) Normalized spectral power distributions of light emitted under three monochromatic light sources. (c) The fluorescent emission chromaticity changes substantially as the light source varies from 400nm to 800nm. This illustration uses fluorescence properties of a real surface obtaining as a mixture of two fluorescent compounds. This surface is analyzed further in the experimental section.

In many cases the fluorescence emission model, $e_{xm,z}$ can be simplifed. First, it was observed by Stokes that the wavelength of the emitted photons is typically longer than that of exciting photons [34]. This implies that $e_{xm,z}(\lambda, \lambda_x) = 0$ if $\lambda \leq \lambda_x$ [44]. Second, in some cases the shape of the fluorescence emission is constant and only its intensity varies with changes in the illumination wavelength (Kasha's rule, [18], also called chromaticity invariance). When this condition holds it has the strong consequence that $e_{xm,z}(\lambda, \lambda_x)$ is a separable function that can be decomposed into a product of two univariate functions $e_{xm,z}(\lambda, \lambda_x) = e_{x,z}(\lambda)e_{m,z}(\lambda_x)$. The function $e_{m,z}(\lambda)$ is called the emission spectrum, which represents the spectral power distribution of the fluorescent light emitted by the surface. The second function $e_{x,z}(\lambda_x)$ is the excitation spectrum, sometimes referred to as the absorption spectrum [31], which describes the efficiency with which incident photons of different wavelengths excite the fluorescence signal. Under these assumptions the fluorescence radiance due to a single fluorophore z may be expressed as

$$\rho_{f,z}(\lambda) = e_{m,z}(\lambda) \int e_{x,z}(\lambda_x)l(\lambda_x)d\lambda_x. \tag{6}$$

The multiplicative relationship between the excitation and emission spectra implies that each of these spectra can be arbitrarily re-scaled and, as long as the reciprocal scaling is applied to the other quantity, the result will remain unchanged. Often both spectra are normalized so that their maximum intensities are equal to one [23], or that the area under the curve is equal to one, i.e. $\int e(\lambda)d\lambda = 1$ [46]. If this is the case an additional intensity scalar needs to be introduced into (6) to reflect these normalizations.

Note that Kasha's rule holds only when the excitation and emission spectra do not overlap. When they do overlap, Stokes shift implies that the emission spectrum will vary with the illumination. Furthermore, the emission spectrum is not invariant when two or more fluorophores are present in a sample; each of the fluorophores will contribute different amounts depending on the illumination. This effect is illustrated in Fig. 1, which shows normalized emission spectra of a surface illuminated with different monochromatic lights and that contains two different fluorophores.

This article has been accepted for publication in a future issue of this journal, but has not been fully edited. Content may change prior to final publication. Citation information: DOI 10.1109/TIP.2020.2973810, IEEE Transactions on Image Processing

A. Discretized image formation model

We represent spectral functions using vectors and matrices quantized to d narrow spectral bins. When a particular surface with n fluorophores is observed using i different camera filters and under j different illuminants the discrete image formation model may be written as

$$M = G \circ C^T \left(\mathbf{diag}(r) + T \circ \sum_{z=1}^{n} e_{m,z} e_{x,z}^T \right) L, \quad (7)$$

with

$$T = \begin{bmatrix} 0 & 0 & & & 0 \\ 1 & 0 & 0 & & \\ 1 & 1 & 0 & & \\ & & & \ddots & \\ 1 & & & 1 & 0 \end{bmatrix}. \quad (8)$$

The $\mathbf{diag}(r)$ operator places the entries of the reflectance vector $r \in \mathbf{R}^d$ along the diagonal of a matrix. The matrix $\sum_{z=1}^{n} e_{m,z} e_{x,z}^T$ with components $e_{m,z}, e_{x,z} \in \mathbf{R}^d$, sometimes called the Donaldson matrix, is a discrete representation of the $e_{xm}(\lambda, \lambda_x)$ function [32]. This matrix is a fluorescent surface analogue of a Lambertian surface's reflectance, *i.e.* it expresses how much of the incident light is radiated in different wavebands. It can be combined with a known illuminant spectral power distribution to estimate the surface radiance. The Donaldson matrix is element-wise multiplied (Hadamard product denoted with $\circ$) with $T \in \mathbf{R}^{d \times d}$, forcing this matrix into a lower triangular form, as predicted by the Stokes rule. The columns of matrix $C = \mathbf{diag}(q_e)\left[s_1, \ldots, s_i\right], C \in \mathbf{R}^{d \times i}$ are formed by filter transmissivities scaled by the sensor quantum efficiency, similarly $L = \left[l_1, \ldots, l_j\right], L \in \mathbf{R}^{d \times j}$ is a matrix whose columns are the illuminant spectral power distributions. The *op*th entry of $G \in \mathbf{R}^{i \times j}$ represents the camera gain parameter associated with the *o*th filter and *p*th illuminant. Finally, the *op*th entry of $M \in \mathbf{R}^{i \times j}$ is the pixel value observed though the *o*th filter and under *p*th illuminant.

Reflectance and fluorescence spectra are typically smooth functions that fall within a low-dimensional subspace spanned by a small number of basis functions [8], [22]. As a consequence any reflectance or fluorescence spectrum can be compactly represented using low dimensional linear models

$$r = B_r w_r, \quad (9)$$

$$e_{x,z} = B_x w_{x,z}, \quad (10)$$

$$e_{m,z} = B_m w_{m,z}, \quad (11)$$

where $B_r \in \mathbf{R}^{d \times n_r}$, $B_x \in \mathbf{R}^{d \times n_x}$ and $B_m \in \mathbf{R}^{d \times n_m}$ are matrices whose columns are basis functions for reflectance, excitation and emission spectra respectively. Similarly $w_r, w_{x,z}, w_{m,z}$ are the corresponding weight coefficient vectors. This modeling approach permits to reduce the number of parameters in the image formation model.

Finally, the compact image formation model, with linear approximations for reflectance, excitation and emission spectra (9) – (11), expresses measured pixel intensities in terms of basis function weights

$$M = G \circ C^T \left(\mathbf{diag}(B_r w_r) + T \circ B_m W B_x^T \right) L, \quad (12)$$

where

$$W = \sum_{z=1}^{n} w_{m,z} w_{x,z}. \quad (13)$$

Note that $\mathbf{rank}(W) = n$ and $W \in \mathbf{R}^{n_m \times n_x}$. This means that the rank of the matrix W is equal to the number of distinct fluorophores present in the sample.

III. ESTIMATION METHODS

Using the image formation model and data, we estimate the reflectance and fluorescence spectra that minimize the Euclidean error between model predictions and measurements M. We propose three estimation algorithms; first, a general method applicable when multiple fluorophores are present in a sample. Second, we simplify the general model for the case when the sample is known to contain a single fluorophore. Third, we show how the single fluorophore model can be simplified even further when only the emission spectrum needs to be estimated.

A. Multi-fluorophore model

The goal of multi-fluorophore estimation is to find such reflectance basis function weights w_r and a matrix W that minimize the Euclidean error in the measurements M subject to physics motivated constraints

$$\begin{aligned} \text{minimize} \quad & \| M - G \circ C^T \left(\mathbf{diag}(B_r w_r) + T \circ B_m W B_x^T \right) L \|_F^2 \\ & + \alpha \| \nabla B_r w_r \|_2^2 + \beta \| \nabla \left(T \circ B_m W B_x^T \right) \|_F^2 \\ & + \beta \| \left(T \circ B_m W B_x^T \right) \nabla^T \|_F^2 \\ \text{subject to} \quad & 0 \leq B_r w_r \leq 1, \\ & 0 \leq T \circ B_m W B_x^T, \\ & \mathbf{rank}(W) = n, \end{aligned} \quad (14)$$

and

$$\nabla = \begin{bmatrix} 1 & -1 & & 0 \\ 0 & 1 & -1 & \\ & & \ddots & \\ 0 & & 1 & -1 \end{bmatrix}, \quad (15)$$

where $\| \cdot \|_F$ is the Frobenius norm of a matrix and the ∇ operator computes differences between adjacent entries in a vector. If we ignore the inequality constraints this problem is a standard ridge regression which provides Maximum-a-posteriori (MAP) estimates of reflectance and fluorescence given the linear image formation model and under spectral smoothness prior.

The objective function is composed of three terms. The first is a data fidelity term that measures the difference between the model and data. Two additional terms, scaled by tuning parameters α and β, encourage smooth solutions by penalizing the objective if neighboring entries in the estimates of the reflectance $B_r w_r$ or the Donaldson matrix $B_m W B_x^T$ vary. In the case of the Donaldson matrix the roughness penalty is imposed on both the rows and columns.

The solution space is further restricted by three constraints. The first constraint follows from the fact that reflectance is

This article has been accepted for publication in a future issue of this journal, but has not been fully edited. Content may change prior to final publication. Citation information: DOI 10.1109/TIP.2020.2973810, IEEE Transactions on Image Processing

a passive process, which does not create new photons. The second constraint is a consequence of nonnegativity of light. Note however that the nonnegativity is applied to the entire Donaldson matrix estimate, not the contributing fluorophore excitation and emission spectra. The third constraint enforces a Donaldson matrix estimate of a particular rank, which is equal to the number of fluorophores present in the sample. The last constraint is cumbersome for two reasons. In general, we do not know in advance how many fluorophores are present in a given sample. Additionally, the rank equality constraint makes the optimization problem non-convex and hard to solve globally.

Instead, we can approximate the original problem by replacing the non-convex constraint with a convex penalty. The rank of a matrix is equal to the number of its nonzero singular values. We can impose a less stringent constraint by penalizing the sum of all the singular values, *i.e.* matrix nuclear norm, which is a convex function [35]. This penalty is analogous to an l_1 penalty applied to matrix singular values, which is typically used to enforce solution sparsity [3], [16]. This penalty will drive the Donaldson matrix estimate towards one that has fewer nonzero singular values, and thus lower rank. This assumption is reasonable because in many practical applications there are only a small number of fluorophores present in the mix. The substitution of nuclear norm penalty for rank constraint produces the following convex relaxation of the original problem

$$\begin{aligned} \text{minimize} \quad & \|M - G \circ C^T \left(\mathbf{diag}(B_r w_r) + T \circ B_m W B_x^T\right) L\|_F^2 \\ & + \alpha \|\nabla B_r w_r\|_2^2 + \beta \|\nabla \left(T \circ B_m W B_x^T\right)\|_F^2 \\ & + \beta \|\left(T \circ B_m W B_x^T\right) \nabla^T\|_F^2 + \eta \|W\|_\star \\ \text{subject to} \quad & 0 \leq B_r w_r \leq 1, \\ & 0 \leq T \circ B_m W B_x, \end{aligned} \tag{16}$$

where $\|W\|_\star$ denotes the nuclear norm of W and η is the penalty tuning parameter. This convex optimization problem, which we will refer to as *multi-fluorophore*, can be efficiently solved using the Alternating Direction Method of Multipliers (ADMM). The solution provides an estimate of the Donaldson matrix, which is the most complete and versatile way to characterize fluorescent properties of a surface containing any number of fluorphores. The multi-fluorophore approach does not explicitly return the non-negative excitation and emission spectra, which would require finding a non-negative Donaldson matrix factorization. The implementation details of the ADMM solver are available in the Supplemental Material (Appendix A). In that appendix we also show how to explicitly enforce the matrix $B_m W B_x$ estimate to have rank n, which might be useful in applications where the number of fluorophores in the mixture is know in advance.

B. Single fluorophore model

When the sample contains only one fluorophore, the estimation problem is substantially simplified: The problem becomes biconvex in the unknown parameters w_r, w_x and w_m. It is possible to strictly enforce the rank constraint $\mathbf{rank}(W) = 1$ by alternating minimization over subsets of parameters in which the objective is convex. Even though the solution algorithm is still iterative, it is easier to solve because the nuclear norm penalty is eliminated from the objective. In addition, the optimization is performed over a single excitation and emission spectrum, which allows to impose nonnegativity directly on those spectra. The *single fluorophore* optimization problem becomes

$$\begin{aligned} \text{minimize} \quad & \|M - G \circ C^T \left(\mathbf{diag}(B_r w_r) + T \circ B_m w_m w_x^T B_x^T\right) L\|_F^2 \\ & + \beta \left(\|\nabla B_x w_x\|_2^2 + \|\nabla B_m w_m\|_2^2\right) \\ & + \alpha \|\nabla B_r w_r\|_2^2 \\ \text{subject to} \quad & 0 \leq B_r w_r \leq 1, \\ & 0 \leq B_x w_x, \\ & 0 \leq B_m w_m, \end{aligned} \tag{17}$$

The optimization is quadratic in w_r, w_m and w_r, w_x. First, a quadratic problem (QP) is solved over the variables w_r, w_m holding w_x's fixed. Next, a QP is solved over w_r and w_x while w_m is fixed. These steps are repeated until no improvement in the objective is observed.

In general there is always a scaling ambiguity in specifying the excitation and emission spectra, which are estimated up to a free multiplicative scale Δ, because $w_x w_m = (w_x/\Delta)(w_m \Delta)$. Despite the scaling uncertainty, the algorithm can still correctly recover the total number of fluoresced photons and relative spectra shapes.

C. Chromaticity invariant model

In some cases a fluorophore emits photons within the one wavelength range, but is excited only by wavelengths below the emission range. This case permits a further simplification because the emission spectrum has the same chromaticity, independent of the light source. This case can be modeled by optimizing over $p = L^T B_x w_x$, $p \in \mathbf{R}^j$ rather than w_x

$$\begin{aligned} \text{minimize} \quad & \|M - G \circ C^T \left(\mathbf{diag}(B_r w_r) L + B_m w_m p^T\right)\|_F^2 \\ & + \beta \|\nabla B_m w_m\|_2^2 + \alpha \|\nabla B_r w_r\|_2^2 \\ \text{subject to} \quad & 0 \leq B_r w_r \leq 1 \\ & 0 \leq B_m w_m \\ & 0 \leq p. \end{aligned} \tag{18}$$

In this chromaticity invariant model (*CIM*) only the shape of the fluorescence emission and an intensity scaling factor are estimated. The scaling factor p_j compactly represents all excitation phenomena for a given illuminant j. The wavelength dependency of the excitation spectrum is not included in the image formation model, it is no longer meaningful to impose the Stokes rule, and the matrix T can be dropped.

IV. ALGORITHM EVALUATION

The proposed estimation algorithms are implemented in Matlab[1]. All three algorithms are iterative in nature. The multi-fluorophore, ADMM solver uses standard matrix operators,

---

[1] The source code is available for download at `https://github.com/hblasins/fiToolbox`, and data at `http://purl.stanford.edu/xc528jd5098`

and the single fluorophore biconvex solver uses the `cvx` convex optimization toolbox [13], [27]. The `cvx` has been designed with versatility, rather than performance in mind, and requires about ~ 1.3 seconds per iteration. The ADMM solver, being tailored towards the specific application, is more computationally efficient and requires only ~ 0.1 second per iteration. The single fluorophore estimation algorithm could be accelerated by moving to an ADMM solver. We use simulations to understand the effect of key system parameters including (a) the number of basis excitation and emission basis functions, (b) the number of illuminants and filters, (c) the robustness to noise, and (d) algorithm convergence rates.

To validate the estimation algorithms, we created synthetic data that comply with the image formation model (7). We used Macbeth chart reflectance spectra and Donaldson matrices from the McNamara-Boswell data set [23], restricted to samples with peak excitation and emission within the 400 to 980nm range. We choose this interval, slightly smaller than the camera spectral range (380 to 1000nm sampled at 4nm, $d = 156$) to eliminate edge cases that may be difficult to analyze. In all evaluation experiments we used 24 test patches, each of which had distinct surface spectral reflectance properties and fluorescence excitation–emission properties of a single fluorescent compound.

We evaluate the accuracy by computing the root-mean-square error, RMSE between estimated and ground truth spectral reflectance curves, Donaldson matrices and excitation and emission spectra. We report the average RMSE and standard deviation over estimates for all test patches in a given experiment. These RMSE quantities typically occupy different ranges. The reflectance values are often around 0.5, while the Donaldson matrix entries rarely exceed 10^{-2}. Consequently, the low absolute values of the RMSE for the Donaldson matrix do not imply superior accuracy but simply capture the level of the fluorescence signal. We refer to all comparisons that preserve the absolute reflectance or fluorescence scales as the *absolute* comparisons. To better match the RMSE scales, we also compute the RMSE for normalized quantities which we will refer to as *normalized* comparisons. In this case the estimate and ground truth are divided by their maximal values before computing the RMSE.

A. Linear model dimensionality

We investigated the model accuracy by varying the number of linear model basis functions. We analyze the approximation for both the excitation and emission spectra. The basis functions were derived from the McNamara-Boswell dataset. We chose five basis to approximate Macbeth chart reflectances, which corresponds to the typically reported dimensionality of that set [43], and is similar to the dimensionality of large sets of natural object surface spectral reflectances [4]. In this experiment we used a bispectral system, where the camera samples spectral bands and the light source generates narrowband light, i.e., $C = L = I$, where $I \in \mathbf{R}^{d \times d}$ is the identity matrix. Camera gain G was adjusted to a maximal pixel intensity of one, and tuning parameters were set to $\alpha = \beta = \eta = 0.001$.

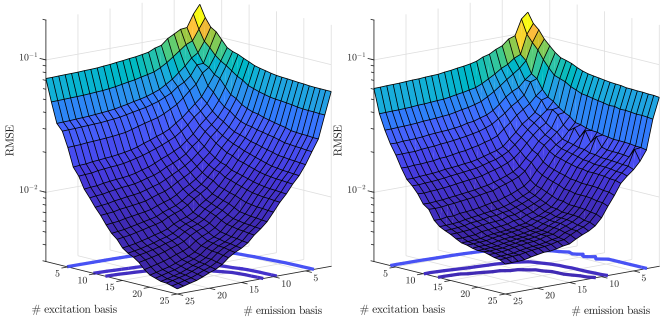

(a) Multi-fluorophore (b) Single fluorophore

Fig. 2: Normalized Donaldson matrix estimation error (RMSE) as a function of the number of linear basis functions approximating excitation and emission spectra. Contour plots show iso-RMSE lines at 0.025, 0.01 and 0.0075.

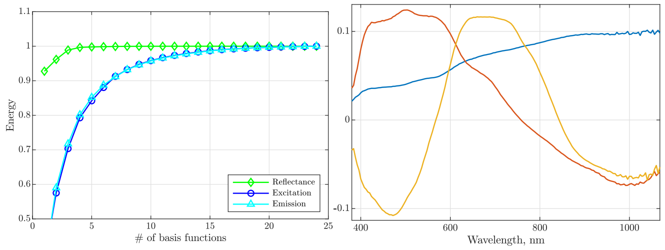

(a) Approximation error (b) Reflectance basis

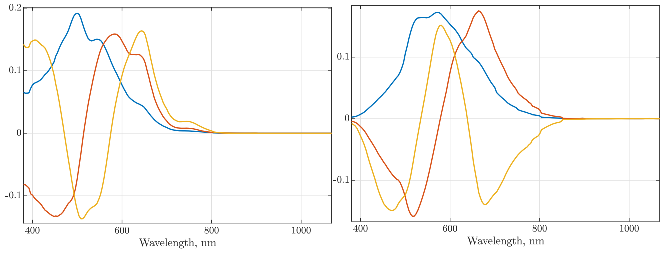

(c) Excitation basis (d) Emission basis

Fig. 3: Linear basis function approximation of spectral quantities. Five reflectance basis functions explain 99% of variance of Macbeth chart reflectances. Similarly, 12 excitation and emission basis functions explain 97% of variance in the McNamara-Boswell data set (a). Remaining panels show three most dominant basis functions for reflectance (b), excitation (c), and emission (d) spectra.

Figure 2 presents the root-mean-square error (RMSE) of the scaled Donaldson matrix estimates using the multi-fluorophore and single fluorophore models averaged over estimates for all test patches. About 12 basis functions provide normalized Donaldson matrix estimate RMSE of the order of 0.01. Furthermore, 12 excitation and emission basis functions account for 97% of variance in the McNamara-Boswell data set (Fig. 3). Based on these calculations, we used 12 excitation and emission bases for subsequent experiments.

B. Number of camera and illuminant channels

We analyzed the impact of the number of camera filters and illuminant channels. To simplify the analysis we investigated

This article has been accepted for publication in a future issue of this journal, but has not been fully edited. Content may change prior to final publication. Citation information: DOI 10.1109/TIP.2020.2973810, IEEE Transactions on Image Processing

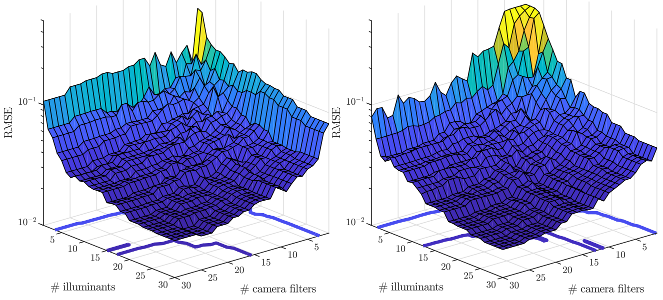

(a) Multi-fluorophore (b) Single fluorophore

Fig. 4: Normalized Donaldson matrix estimation error (RMSE) as a function of the number of camera filters and illuminants. The number of linear bases used to approximate the excitation and emission spectra was set to 12. Contour plots show iso-RMSE lines at 0.05 and 0.02.

how to allocate the entire available spectrum between camera and illuminants. We assumed that camera filters and illuminant spectral profiles were rectangular, and their widths were adjusted so that the sum of all channels produced a flat response over the entire spectral range. For a specific number of camera channels and illuminants the performance will also depend on the shapes and positions of camera spectral sensitivity and illuminant emission spectra. Such analyses can be conducted using the simulation tools from the repository.

Just as before we set the tuning parameters to $\alpha = \beta = \eta = 0.001$. Figure 4 presents the RMSE of the Donaldson matrix estimates averaged over 24 different fluorophores. Using about 20 filters and illuminants produced normalized RMSE on the order of 0.02. The error surfaces in Fig. 4 are less smooth, compared to those obtained by varying the number of basis functions, because we did not vary the spectral shapes and pass-band positions of camera filters and illuminants.

C. Parameter selection

Three tuning parameters (α, β and η) govern the smoothness of the spectral estimates. We conducted experiments that varied the tuning parameters over a large range of values, and measured estimation errors (see Supplemental Material, Appendix C). Small changes in the values of these parameters do not have a large impact on the overall accuracy of the estimate, but they have an impact on which aspect of the model accounts for most of the error. Using simulations the parameters can be adapted for a particular system architecture (illuminant spectra, camera spectral sensitivities, and expected fluorophores).

D. Noise performance

We analyzed the estimation accuracy in the presence of noise. We fixed tuning parameters to $\alpha = \beta = \eta = 0.01$, and added different amounts of Gaussian noise to the simulated pixel intensities M. At each noise level and for each of the 24 samples we used 10 different instances of noise patterns, producing 240 estimates per noise level. Figure 5 shows the average RMSE of the Donaldson matrix, reflectance, and pixel values estimates as a function of the signal to noise ratio (SNR). The error bars represent standard errors computed for the 10 noise instances and averaged over 24 samples. The accuracy asymptotes with the SNR reaching 10dB.

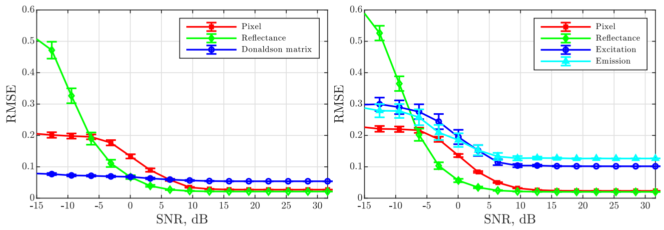

(a) Multi-fluorophore (b) Single fluorophore

Fig. 5: Estimation accuracy in the presence of noise. Each curve shows the reduction in RMSE as the SNR increases for multi (a) and single (b) fluorophore estimation algorithms. In both cases the estimation accuracy asymptotes as SNR approaches 10dB.

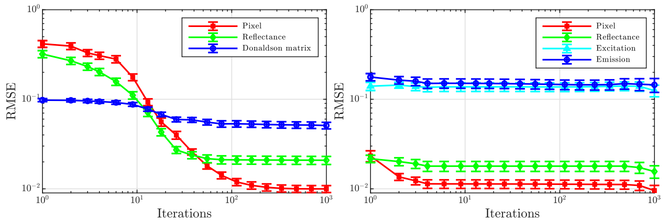

(a) Multi-fluorophore (b) Single fluorophore

Fig. 6: Estimation accuracy with increasing number of algorithm iterations. The multi-fluorophore method (a) converges to a solution more slowly than the single fluorophore algorithm (b).

E. Algorithm convergence

Finally, we tested the estimation accuracy for different number of algorithm iterations. Figure 6 presents the multi-fluorophore estimates RMSE as a function of the number of ADMM iterations as well as the single fluorophore estimates RMSE as a function of the number of biconvex iterations. Algorithm parameters were set to $\alpha = \beta = \eta = 0.01$. All curves are averaged over estimates for 24 different fluorophores and reflectance spectra. The multi and single fluorophore estimates of the reflectance and pixel values converge to approximately the same RMSE values. The multi-fluorophore ADMM method converges much more slowly than the single fluorophore, biconvex solver.

V. SYSTEM EVALUATION

We implemented a custom fluorescence imaging system and applied the algorithms to the data from this system. These experiments evaluate the algorithms in a setting where noise, calibration accuracy and other sources of uncertainty are non-negligible, .

In all computations we use five basis functions derived from the set of Macbeth chart reflectances [43] and 12 basis for

This article has been accepted for publication in a future issue of this journal, but has not been fully edited. Content may change prior to final publication. Citation information: DOI 10.1109/TIP.2020.2973810, IEEE Transactions on Image Processing

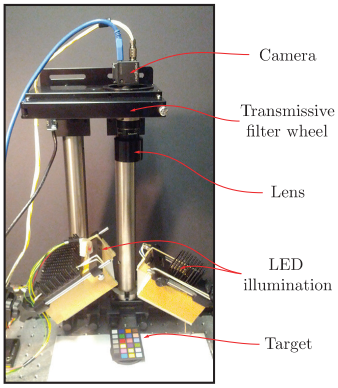

(a) Overview

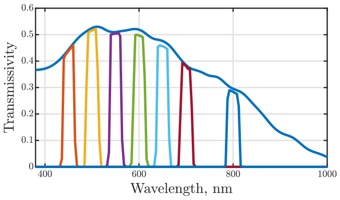

(b) Filters

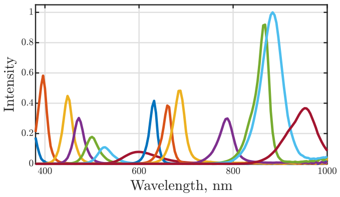

(c) Illuminants

Fig. 7: The experimental image acquisition system. (a) A monochrome, PointGrey Flea3 FL3-U3-13Y3M-C, 1.3MP camera with a Schneider Optics Tele-Xenar 70mm lens. (b) The system acquires images through one broadband and seven 25mm bandpass filters centered at 450, 500, 550, 600, 650, 700 and 800nm. The filters are housed inside an Edmund Optics motorized filter wheel placed between the camera and the lens. (c) The scenes are illuminated by one of 14 narrowband, LED illuminants. The LEDs with $350 - 400$nm peaks were manufactured by International Light Technologies, the $400-700$nm LEDs were from Luxeon, and the $700 - 950$nm LEDs from Epitex. Filter wheel positions and illumination times are synchronized using an Arduino Mega2560 controller. To reduce illuminant spatial non-uniformity we inserted glass diffusers in front of the LED light sources. We further estimated this non-uniformity by capturing a calibration image of a block of magnesium oxide (chalk).

excitation and emission spectra, derived from the McNamara-Boswell data set [23]. The choice of tuning parameters (α, β and η) had little influence on the algorithm accuracy over a broad range of values; therefore, we adjusted them manually, rather than through rigorous cross-validation (see Supplemental Material, Appendix C).

A. System architecture

The system comprises eight different camera filters and 14 LED illuminants with peak emission spectra in the 350 to 950nm range Fig. 7. The Donaldson matrix estimation errors for this system for multi-fluorophore and single fluorophore algorithms are of the order of 0.04 (Fig. 4). A single acquisition consists of a collection of captures for every filter–illuminant pair. In the Supplemental Material (Appendix B) we show an example scene acquired with our system.

B. Targets

In our experiments we used two types of targets. The first target type was modular and enabled us to systematically vary the number and combinations of fluorophores in a principled and controlled way. Targets of the second type represented materials encountered in real life: fluorescent dyes applied to different substrates.

Targets of the first type were composed of two, individually calibrated, building blocks; a purely reflective Macbeth color test chart and semi-transparent fluorescent microscopy slides from Chroma Technology Corporation[2]. The slides were placed on top of the Macbeth chart to create targets with a range of reflectance and fluorescence properties. We created two targets of the first type by varying the number of fluorophore slides placed on top of the Macbeth chart. The number of slides stacked on top of each other defined the number of fluorophores. We used the chart plus one or two slides to evaluate the multi-fluorophore method. We used the chart and one slide to evaluate single fluorophore algorithm (Fig. 8).

The second type of targets were mixtures of commercially available fluorescent dyes applied on a substrate. One multi-fluorophore target was created by applying two fluorescent dyes; ‘red’ and ‘green,’ onto a piece of white fabric. The fabric was painted so that some areas contained only one dye, but there was also an area where both dyes were present. Another target, created in a similar way with different dyes is described and analyzed in Supplemental Material.

C. Calibration

The system and targets were calibrated in the 380nm to 1000nm range at 4nm increments. We used a SpectraScan PR715 spectrophotometer to measure radiance, and an Oriel Cornerstone 130 monochromator to produce narrowband illuminants.

Spectral power distributions of the LEDs were estimated by measuring the radiance off a diffuse white, Spectralon target illuminated with each LED. We used the approach of [36] to measure camera spectral responsivity function. We estimated the Macbeth, and other reflectances using standard procedures of illuminating with a broadband light and measuring the returned radiance.

We estimated the fluorescence and transmissivity of the fluorescent slides using gold-standard bispectral methods; *i.e.* we illuminated the slide with monochromatic light and measured the spectral radiance. We computed the fluorescent emission spectrum by illuminating with a short wavelength light (360nm) and using the measured radiance as the approximate fluorescent emission spectrum. We used the known emission as the single element basis function in the multi-fluorophore algorithm (16) which we applied to estimate the transmittance and excitation. When assembling the multi-element test target (Fig. 8) we would correct the estimated Macbeth chart reflectance by the transmission characteristic of fluorescent slides placed on top of each patch. Natural targets (fabrics and dyes) could not be physically separated into reflective and fluorescent components. In those cases we also used the gold standard bispectral methods with small number of basis functions.

---

[2] https://www.chroma.com/products/filter-accessories/diagnostic-slides

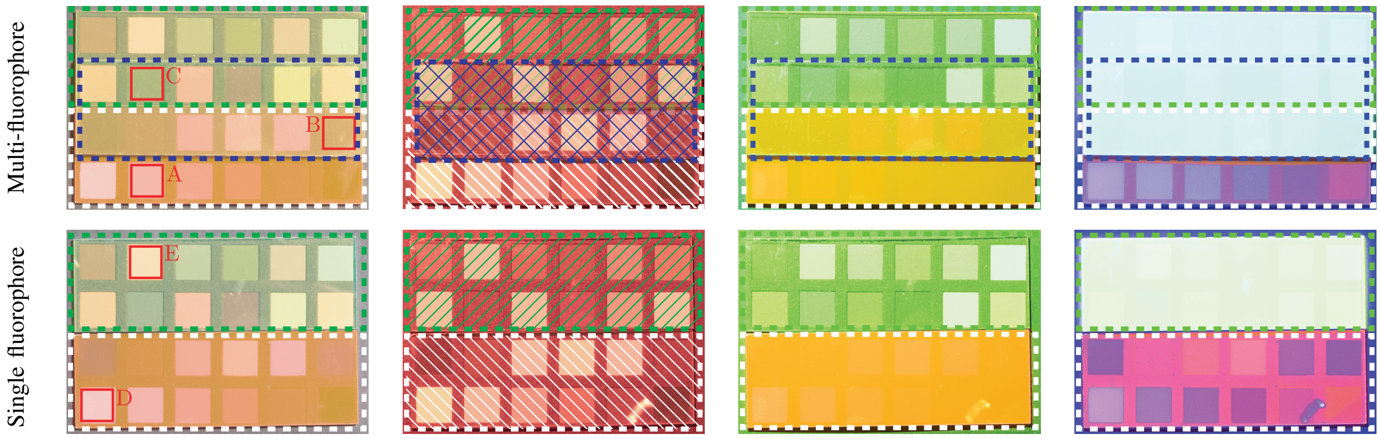

(a) Tungsten (b) Red LED (c) Green LED (d) Blue LED

Fig. 8: Conventional color camera images of the test target composed of fluorescent slides placed on top of a reflective Macbeth chart. Different slide boundaries are marked with dashed lines (their areas are further shaded in column b for clarity). The multi-fluorphore configuration (top) has two layers of slides placed over middle rows of the Macbeth chart (blue dashed line). In the single fluorophore configuration (bottom) fluorescent slides form a single layer. Columns present the appearance of the targets under different light sources (a) tungsten, (b) red, (c) green, and (d) blue LEDs. The fluorescence and reflectance of patches labeled A–E in (a) is further analyzed in Fig. 9 and 11. The fluorescent slides are transparent under red light (b), but emit photons in the orange and green bands, when illuminated with green and blue light respectively (c,d). Note that the patch B changes color from green to orange when the illuminant changes from blue to green, and thus violates the chromaticity invariance principle.

TABLE II: Comparison between multi-fluorophore algorithms. The RMSE ± 1 sd are shown. Suo et al. [35] represent reflectance as a square matrix. Although their estimate sometimes includes non-zero off-diagonal terms, we estimate the RMSE reflectance error using only the diagonal terms.

Quantity / Algorithm	Pixel values	Reflectance	Donaldson matrix	
			Absolute $\times 10^{-2}$	Normalized
Ours – Multi-fluorophore	$\mathbf{0.02 \pm 0.00}$	$\mathbf{0.07 \pm 0.03}$	$\mathbf{0.08 \pm 0.01}$	$\mathbf{0.09 \pm 0.02}$
Suo et al. [35]	$\mathbf{0.02 \pm 0.00}$	0.40 ± 0.18	0.13 ± 0.01	0.21 ± 0.04

D. Estimation

To estimate algorithm robustness against noise in real captures we use bootstrapping to calculate the 95% confidence intervals on the estimated curves [6]. Given a particular test patch we run the estimation algorithms 100 times using pixel values randomly drawn, with replacement, from the image area representing that patch. Confidence interval boundaries are given by the 2.5th and 97.5th percentiles of estimate distributions at a particular wavelength.

1) Multi-fluorophore estimation: We evaluate the multi-fluorophore estimation algorithm using 24 test patches containing one or two superimposed fluorophores (Table II). Figure 9 shows spectral estimates and ground truth data for three patches outlined on the test chart presented in Fig. 8. Patch A contains single 'orange' fluorophore, patch B is a mixture of 'orange' and 'green' fluorophores and patch C is a mixture of 'green' and 'amber' fluorophores.

We used the multi-fluorophore method with tuning parameters $\alpha = 0.1$, $\beta = 10$, $\eta = 0.01$ to perform spectral estimation. Our algorithm correctly determines that patch A contains a single fluorophore with the emission peak around 600nm and the excitation peak above 500nm. The the Donaldson matrix estimate for patch B is bimodal. The estimate contains the orange fluorophore peak at 600nm emission wavelength, just like the estimate for patch A, and another peak representing the green fluorophore, with the emission around 500nm. In case of patch C the spectral distinction between green and amber fluorophores is small (Fig. 8d). For this reason the Donaldson matrix estimate is unimodal.

Once the image is separated into reflected and fluoresced components, we can predict the returned radiance when the object is illuminated by arbitrary lights (scene relighting). Figure 10 shows the second test target, composed of a white piece of cloth painted with two fluorescent dyes. We illuminated the target with lights generated by a Thouslite LEDCube[3] and captured images with a Canon G7X consumer camera. We also used an accurate model of the camera and the ground truth material characteristics to predict the scene radiance, and consequently the RGB pixel values of captured images. Simulation tools offer greater flexibility in scene manipulation and enable to easily separate reflected and fluoresced photons, or to model scene appearance under different illuminants.

Figure 10 also shows a comparison between estimated and ground truth fluoresced radiance due to different compounds.

---

[3] http://www.thouslite.com/show.asp?id=16

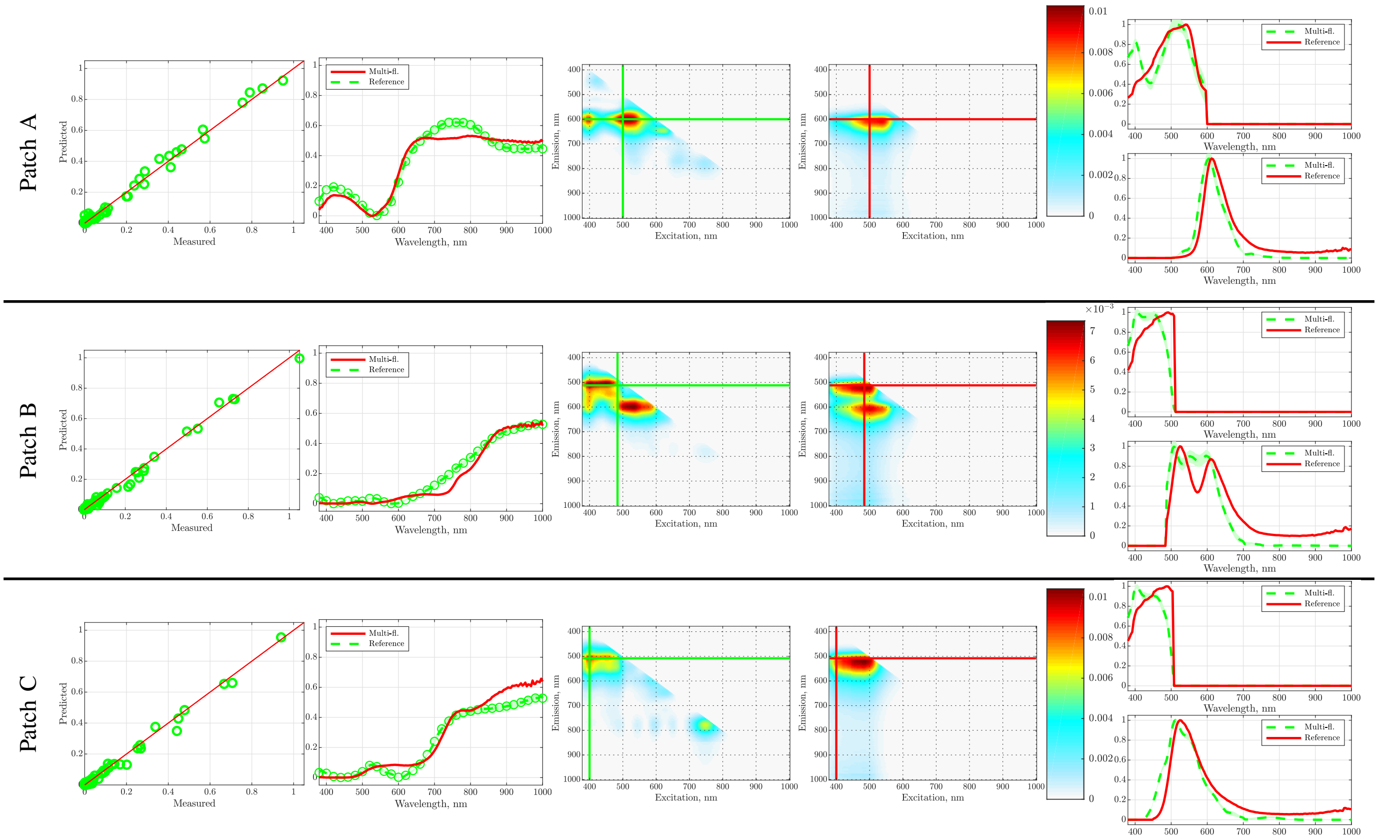

(a) Pixels (b) Reflectance (c) Donaldson estimate (absolute) (d) Donaldson reference (absolute) (e) Spectra (normalized)

Fig. 9: Multi-fluorophore estimation results for patches A, B and C outlined in Fig. 8a. Columns show the estimates and ground truth reference for pixel values (a) reflectance (b) the Donaldson matrix (c,d) and (e) the Donaldson matrix cross-sections along rows and columns (c, green lines; d, red lines). Shaded areas denote the 95% confidence intervals. Patch A contains one, while patches B and C two fluorophores. The separation between orange and green fluorophores in patch B is clearly visible, as the Donaldson matrix estimate is bi-modal. The green and amber fluorophores in patch C have similar emission spectra, and thus disguise as a single fluorescent compound.

Note that our approach accurately predicts the peak emission and shape of radiance emitted by single fluorophore patches F and G. The estimated radiance fluoresced by patch H, which contains both fluorescent compounds, reflects the presence of both fluorophores through its bimodal character. The radiance has two peaks located at the emission wavelengths of individual fluorescent compounds. Note that when the illumination is altered (patch H*) the relative heights of those peaks change causing a shift in chromaticity and thus violating the chromaticity invariance assumption. We compared the multi-fluorphore method with an adapted version of the nuclear norm minimization approach of Suo *et al.* [35], (Supplemental Material, Appendix F), which we implemented in Matlab. Suo *et al.* [35] include a tuning parameter that sets a bound on the pixel prediction error. We adjusted this parameter so that the error in measured pixel intensities is the same as in our multi-fluorophore approach. The high accuracy in pixel value predictions does not translate to accurate reflectance and Donaldson matrix estimates. For the same pixel error, our method produces more accurate Donaldson matrix and reflectance estimates.

2) Single fluorophore estimation: We use the single fluorophore and CIM models to analyze the target with one fluorophore ($\alpha = 0.01$ and $\beta = 0.1$). The β value is reduced compared to the multi-fluorophore setting because the two methods compute smoothness of excitation end emission spectra only, rather than every row and column of the Donaldson matrix. In our case the Donaldson matrix contains 156 rows and columns, which explains the two order of magnitude difference in the value of β.

Figure 11 shows the estimated pixel values, reflectance and fluorescence excitation and emission spectra of patches D and E (Fig. 8a). Both algorithms accurately model the measured pixel intensities and provide good estimates of the reflectance, excitation and emission spectra shapes as well as intensity scales. The estimates are reliable and repeatable, as indicated by the 95% confidence intervals. Table III summarizes the average error (RMSE) over 24 test patches. The single fluorophore and CIM algorithms achieve similar RMSE scores. The CIM approach does not recover the excitation spectra, but it more accurately estimates the fluorescence emission. We compare the single-fluorophore algorithm to our

This article has been accepted for publication in a future issue of this journal, but has not been fully edited. Content may change prior to final publication. Citation information: DOI 10.1109/TIP.2020.2973810, IEEE Transactions on Image Processing

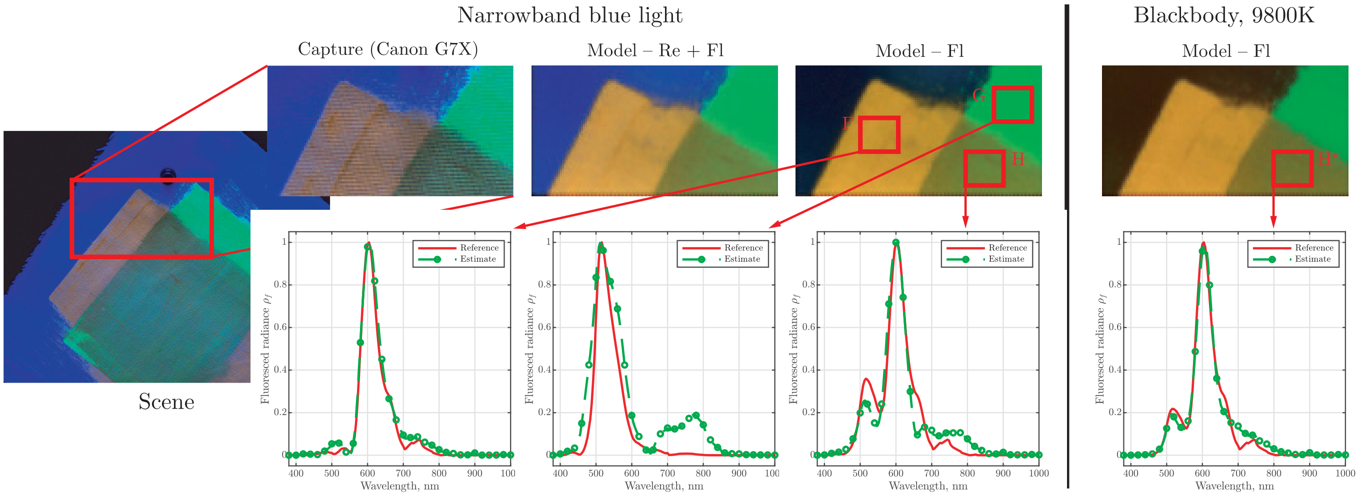

Fig. 10: Fluoresced and reflected radiance separation and relighting. A natural test target containing multiple fluorophores was captured with a consumer camera (Canon G7 X) under a narrowband blue illuminant (Capture, top row). This target was also imaged using our system and the proposed multi-fluorophore algorithm was used to estimate surface properties. These estimates, together with the illuminant spectrum and an accurate model of a Canon G7 X, were used to predict the RGB pixel intensities of the camera output. We show two such predictions, the first one demonstrates predicted RGB pixel values for the same scene and conditions (Model–Re+Fl). The second one shows the RGB contributions of only the radiance fluoresced from the scene, and ignores the reflected component (Model–Fl). Such an image would be difficult to obtain in practice. The bottom row compares the radiance emitted by fluorescent compounds F, G and H modeled using ground truth material properties (red) and predicted using material property estimates obtained with the multi-fluorophore algorithm (green). The radiance estimate for patch H, a mixture of fluorophores from F and G, has a bimodal character. The modes are aligned with peak emissions of fluorophores from patches F and G. The appearance of that patch is also simulated under a blackbody radiator at 9800K (H*). A change in illumination causes an increase in the relative height of fluoresced radiance peaks causing a chromaticity shift.

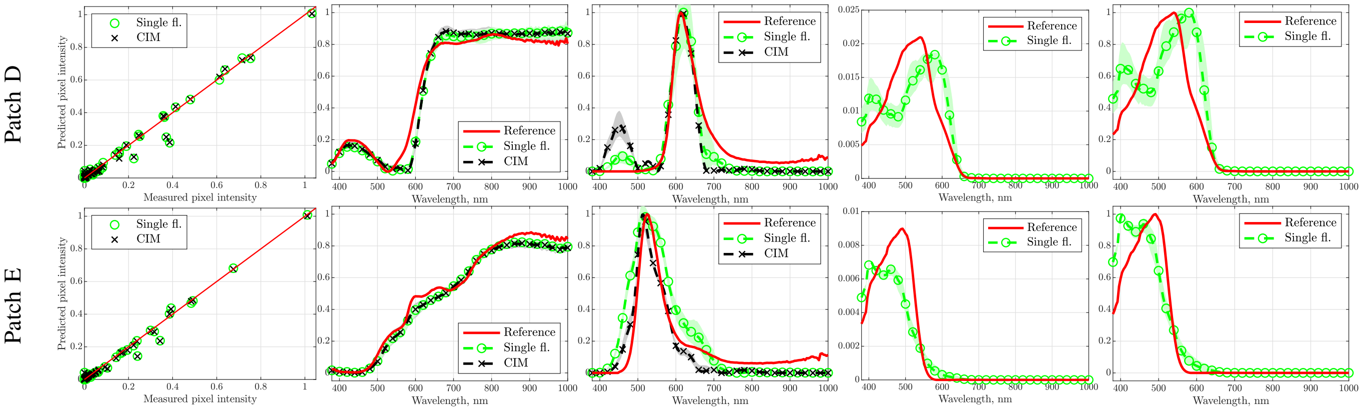

(a) Pixels (b) Reflectance (c) Emission (d) Excitation (absolute) (e) Excitation (normalized)

Fig. 11: Single fluorophore estimates. A row of panels represents estimates for a single test patch and each panel compares true (solid) and estimated (dashed) pixel intensities (a), reflectance (b), emission (c), absolute excitation (d), and normalized excitation (e). The shaded areas represent 95% confidence intervals around the estimates.

implementation of the method by Fu *et al.* [8], which we also include in our code base. Our approach has smaller errors (RMSE) compared to Fu *et al.* [8], [10] (Table III), who uses a sequence of optimizations, while the single fluorophore and chromaticity invariant (CIM) methods solve with a single optimization step. It is likely that the single step optimization avoids error accumulation across separate steps and leads to a performance increase.

VI. DISCUSSION

The CIM algorithm produces the most accurate emission spectra estimates, though it does not return the excitation spectrum estimate. CIM achieves this accuracy by solving an optimization problem that allows independent scaling of the fluorescence emission under every illuminant. The other multi- and single fluorophore approaches couple the fluorescent scaling through the excitation spectrum, which reduces the accuracy slightly (Table III). The multi-fluorophore approach

TABLE III: Comparison of single fluorophore estimation algorithms. The RMSE ± 1 sd are shown.There is a scaling ambiguity between the excitation and emission spectra; without loss of generality we assume that the peak emission spectrum is scaled to a value of 1 and that the fluorescence intensity is contained entirely within the scale of the excitation spectrum. Hence, we include the RMSE of the absolute and normalized excitation estimate, but there is no need to do so for the emission spectrum.

Quantity Algorithm	Pixel values	Reflectance	Emission	Excitation	
				Absolute $\times 10^{-1}$	Normalized
Ours – CIM	$\mathbf{0.02 \pm 0.00}$	0.05 ± 0.03	$\mathbf{0.09 \pm 0.02}$	–	–
Ours – Single fluorophore	$\mathbf{0.02 \pm 0.00}$	$\mathbf{0.04 \pm 0.02}$	0.14 ± 0.05	$\mathbf{0.03 \pm 0.02}$	$\mathbf{0.15 \pm 0.04}$
Fu et al. [8]	0.07 ± 0.02	0.26 ± 0.17	0.28 ± 0.13	0.12 ± 0.09	0.30 ± 0.12

provides Donaldson matrix estimates, which jointly describes the effects of all fluorescent compounds present in the sample. The Donaldson matrix description is sufficient to predict the fluorescent signal radiated by a sample, but it does not explicitly derive individual excitation and emission spectra of each of the constituent fluorophores.

When two or more fluorophores with distinct emission spectra are present, the proposed imaging system, combined with the multi-fluorophore approach, correctly identifies the multimodal character of the Donaldson matrix (Fig. 9, patches A, B). When the fluorescent emission spectra overlap, the multi-fluorophore approach produces a unimodal estimate, which can be confused with a single fluorophore case (patch C).

The experimental accuracy is limited by the imaging system, rather than the algorithms; the simulations demonstrate that resolution can be increased with systems that include a larger number of imaging channels and/or illuminants (Fig. 4). Simulations also confirm the algorithms robustness against noise. We can consider a capture under one illuminant–camera pair as a single observation in a noisy environment. The acquisition sequence consists of many captures with different, and approximately independent, noise realizations. This acquisition scenario works well with an algorithm that returns a Maximum–a–Posteriori (MAP) estimate, and thus produces results that are resilient against noise.

The algorithms accuracy is not strongly dependent on the tuning parameters (α, β, η), but the parameters are coupled by distributing the sources of the error. An adjustment that changes the reflectance estimate will impact the fluorescence estimate. This is because the system observes the total reflected and fluorescent radiance. Increasing the smoothness of of one component will change the estimate in a different component.

Knowledge of the reflectance and fluorescence properties allow us to predict the spectral radiance under different illuminants (Fig. 10). We evaluated the accuracy of this calculation by capturing images of the same object under the simulated illumination conditions. The measured and predicted camera images are accurate to about 5%, with much of the error being due to surface unevenness and spatial light non-uniformity. We note that the present algorithms operate independently on each pixel, and it is likely that additional spatial constraints, such as a total variation prior, may improve performance. Although this greatly increases the size of the calculation, early tests show that the spatial constraints can be incorporated and solved with the Alternating Direction Method of Multipliers [2].

We note some practical issues relating to system performance. To determine the correct scales of fluoresced and reflected radiances the camera has to be accurately calibrated over all gains (ISO), photo response non-uniformity, shutter speed and aperture settings. High power LEDs produce significant amounts of heat which, if not dissipated, affects light output and causes wavelength shifts in the illuminant spectrum. These calibration errors have smaller impact on estimating the shapes of excitation and emission spectra, but they greatly influence the measurements of absolute spectral levels.

VII. CONCLUSIONS

We present a unified framework for simultaneous estimation of surface reflectance and fluorescence properties. We show how to derive these properties from a small number of images taken with different narrowband filters and under narrowband illuminants. Our image formation model makes few assumptions regarding the properties of fluorescence emission and can account for multiple fluorophores present in the sample. We show how the general, multi-fluorophore estimation algorithm can be further simplified when it is known that only one fluorescent compound is present in the sample. The simplified single fluorophore and CIM models are more computationally efficient.

We built an imaging system to evaluate the algorithms. The system uses bandpass filters, LEDs and a CMOS sensor that can be easily integrated into imaging devices operating at micro and macro scales. Our algorithms produce lower errors compared to earlier algorithms.

We frame reflectance and fluorescence estimation as inverse estimation problems and use convex optimization techniques to search for solutions. Such formulations allow easy algorithmic modifications, when for example, fluorescence emission properties are known and only their amounts need to be quantified. Future directions of research could be directed towards estimating excitation–emission spectra of individual fluorophores, rather than the Donaldson matrix of their mixture. The emergence of learning driven approaches provides an interesting framework for reflected and fluoresced component separation.

REFERENCES

[1] M. Alterman, Y. Schechner, and A. Weiss. Multiplexed fluorescence unmixing. In *Proceedings of the IEEE International Conference on Computational Photography, ICCP*, pages 1–8, March 2010.

[2] H. Blasinski, J. Farrell, and B. Wandell. An iterative algorithm for spectral estimation with spatial smoothing. In *Proceedings of the IEEE International Conference on Image Processing, ICIP*, October 2015.

[3] A. Bruckstein, D. Donoho, and M. Elad. From sparse solutions of systems of equations to sparse modeling of signals and images. *SIAM Review*, 51(1):34–81, 2009.

[4] C. Chiao, T. Cronin, and D. Osorio. Color signals in natural scenes: characteristics of reflectance spectra and effects of natural illuminants. *Journal of the Optical Society of America A*, 17(2):218–224, February 2000.

[5] N. Dimitriadis, B. Grychtol, L. Maertins, T. Behr, G. Themelis, and N. Deliolanis. Simultaneous real-time multicomponent fluorescence and reflectance imaging method for fluorescence-guided surgery. *Opt. Lett.*, 41(6):1173–1176, March 2016.

[6] B. Efron and R. Tibshirani. Bootstrap methods for standard errors, confidence intervals, and other measures of statistical accuracy. *Statistical Science*, pages 54–75, 1986.

[7] J. Farrell, F. Xiao, P. Catrysse, and B. Wandell. A simulation tool for evaluating digital camera image quality. In *Electronic Imaging 2004*, pages 124–131. International Society for Optics and Photonics, 2003.

[8] Y. Fu, A. Lam, Y. Kobashi, I. Sato, T. Okabe, and Y. Sato. Reflectance and fluorescent spectra recovery based on fluorescent chromaticity invariance under varying illumination. In *Proceedings of the IEEE Conference on Computer Vision and Pattern Recognition, CVPR*, pages 2171–2178, June 2014.

[9] Y. Fu, A. Lam, I. Sato, T. Okabe, and Y. Sato. Separating reflective and fluorescent components using high frequency illumination in the spectral domain. In *Proceedings of the IEEE International Conference on Computer Vision, ICCV*, pages 457–464, August 2013.

[10] Y. Fu, A. Lam, I. Sato, T. Okabe, and Y. Sato. Reflectance and fluorescence spectral recovery via actively lit RGB images. *IEEE Transactions on Pattern Analysis and Machine Intelligence*, 38(7):1313–1326, 2016.

[11] E. Fuchs. Separating the fluorescence and reflectance components of coral spectra. *Applied optics*, 40(21):3614–3621, 2001.

[12] I. Georgakoudi, B. Jacobson, J. Van Dam, V. Backman, M. Wallace, M. Müller, Q. Zhang, K. Badizadegan, D. Sun, G. Thomas, et al. Fluorescence, reflectance, and light-scattering spectroscopy for evaluating dysplasia in patients with barrett's esophagus. *Gastroenterology*, 120(7):1620–1629, 2001.

[13] M. Grant and S. Boyd. CVX: Matlab software for disciplined convex programming, version 2.1. http://cvxr.com/cvx, Mar. 2014.

[14] D. Gray, W. Merigan, J. Wolfing, B. Gee, J. Porter, A. Dubra, T. Twietmeyer, K. Ahmad, R. Tumbar, F. Reinholz, and D. Williams. In vivo fluorescence imaging of primate retinal ganglion cells and retinal pigment epithelial cells. *Opt. Express*, 14(16):7144–7158, August 2006.

[15] F. Grum and J. Bartleson. *Optical radiation measurements, Volume 2 Color Measurement*. Academic Press, 1980.

[16] T. Hastie, R. Tibshirani, and J. Friedman. *The Elements of Statistical Learning*. Springer, 2009.

[17] H. Ikoma, B. Heshmat, G. Wetzstein, and R. Raskar. Attenuation-corrected fluorescence spectra unmixing for spectroscopy and microscopy. *Optics Express*, 22(16):19469–19483, 2014.

[18] M. Kasha. Characterization of electronic transitions in complex molecules. *Discussions of the Faraday Society*, 9:14–19, 1950.

[19] T. Kim, K. Cho, E. Lee, S. Lee, J. Chae, J. Kim, D. Kim, J. Kwon, G. Amaratunga, S. Lee, et al. Full-colour quantum dot displays fabricated by transfer printing. *Nature Photonics*, 5(3):176–182, 2011.

[20] J. Lakowicz. *Principles of Fluorescence Spectroscopy*. Kulwer Academic/Plenum Publishers, 1999.

[21] A. Lam and I. Sato. Spectral modeling and relighting of reflective-fluorescent scenes. In *Proceedings of the IEEE Conference on Computer Vision and Pattern Recognition, CVPR*, pages 1452–1459, June 2013.

[22] L. Maloney and B. Wandell. Color constancy: a method for recovering surface spectral reflectance. *Journal of the Optical Society of America A*, 3(1):29–33, 1986.

[23] G. McNamara, A. Gupta, J. Reynaert, T. Coates, and C. Boswell. Spectral imaging microscopy web sites and data. *Cytometry*, 69A(8):863–871, 2006.

[24] I. Medintz, T. Uyeda, E. Goldman, and H. Mattoussi. Quantum dot bioconjugates for imaging, labelling and sensing. *Nature Materials*, 4(6):435–446, 2005.

[25] D. Mitchell, G.and Kiefer. Chlorophyll α specific absorption and fluorescence excitation spectra for light-limited phytoplankton. *Deep Sea Research Part A. Oceanographic Research Papers*, 35(5):639–663, 1988.

[26] M. Monici. Cell and tissue autofluorescence research and diagnostic applications. *Biotechnology Annual Review*, 11:227–256, 2005.

[27] J. Nocedal and S. Wright. *Numerical Optimization*. Springer, 2006.

[28] V. Ntziachristos, C. Bremer, and R. Weissleder. Fluorescence imaging with near-infrared light: new technological advances that enable in vivo molecular imaging. *European Radiology*, 13(1):195–208, 2003.

[29] J. Park, M. Lee, M. D. G., and S. Nayar. Multispectral imaging using multiplexed illumination. In *Proceedings of the IEEE International Conference on Computer Vision, ICCV*, pages 1–8, October 2007.

[30] M. Parmar, S. Lansel, and J. Farrell. An LED-based lighting system for acquiring multispectral scenes. In *Digital Photography VIII*, volume 8299, pages 211–218, 2012.

[31] D. Rendell. *Fluorescence and Phosphorescence*. John Wiley & Sons, 1987.

[32] U. Resch-Genger. *Standardization and quality assurance in fluorescence measurements I: Techniques*, volume 6 of *Springer Series on Fluorescence*. Springer, 2008.

[33] R. Rodieck. *The First Steps in Seeing*. Sinauer Associates, 1998.

[34] G. Stokes. On the change of refrangibility of light. *Philosophical Transactions of the Royal Society of London*, 142:463–562, 1852.

[35] J. Suo, L. Bian, F. Chen, and Q. Dai. Bispectral coding: compressive and high-quality acquisition of fluorescence and reflectance. *Optics Express*, 22(2):1697–1712, January 2014.

[36] Q. Tian, H. Blasinski, S. Lansel, H. Jiang, M. Fukunishi, F. J., and B. Wandell. Automatically designing an image processing pipeline for a five-band camera prototype using the local, linear, learned (L^3) method. In *Digital Photography XI*, volume 9404, pages 18–23, February 2015.

[37] Q. Tian and R. Chung. A study of optical brightening agents (OBA) correction methods. *Advanced Materials Research*, 174:346–349, 2011.

[38] S. Tominaga, K. Hirai, and T. Horiuchi. Estimation of bispectral matrix for fluorescent objects. In *Proceedings of the Colour and Visual Computing Symposium, CVCS*, pages 1–4, September 2013.

[39] S. Tominaga, K. Hirai, and T. Horiuchi. Estimation of bispectral donaldson matrices of fluorescent objects by using two illuminant projections. *Journal of the Optical Society of America A*, 32(6):1068–1078, June 2015.

[40] S. Tominaga, T. Horiuchi, and T. Kamiyama. Spectral estimation of fluorescent objects using visible lights and an imaging device. In *Proceedings of the Color and Imaging Conference*, pages 352–356, January 2011.

[41] T. Treibitz, B. Neal, D. Kline, O. Beijbom, P. Roberts, G. Mitchell, and D. Kriegman. Wide field-of-view fluorescence imaging of coral reefs. *Scientific reports*, 5, 2015.

[42] A. Waggoner. Fluorescent labels for proteomics and genomics. *Current Opinion in Chemical Biology*, 10(1):62–66, 2006.

[43] B. Wandell. *Foundations of Vision*. Sinauer Associates, 1995.

[44] G. Wyszecki and W. Stiles. *Color Science*. John Wiley & Sons, 1982.

[45] D. Zawada and C. Mazel. Fluorescence-based classification of caribbean coral reef organisms and substrates. *PLoS ONE*, 9(1):1–13, January 2014.

[46] C. Zhang and I. Sato. Separating reflective and fluorescent components of an image. In *Proceedings of the IEEE Conference on Computer Vision and Pattern Recognition, CVPR*, pages 185–192, June 2011.

[47] Y. Zheng, Y. Fu, A. Lam, I. Sato, and Y. Sato. Separating fluorescent and reflective components by using a single hyperspectral image. In *Proceedings of the IEEE International Conference on Computer Vision, ICCV*, pages 3523–3531, 2015.

[48] Y. Zheng, I. Sato, and Y. Sato. Spectra estimation of fluorescent and reflective scenes by using ordinary illuminants. In *Proceedings of the European Conference on Computer Vision, ECCV*, pages 188–202. Springer, 2014.

Henryk Blasinski Henryk Blasinski (S'10) received the M.S. degree (Hons.) in telecommunications and computer science from the Lodz University of Technology, Lodz, Poland, and the Diplome d'Ingeneiur degree from the Institut Superieur d'Electronique de Paris, France, in 2008 and 2009, respectively, and a Ph. D. degree from the Department of Electrical Engineering, Stanford University, CA in 2018. He was a Fulbright Scholar with the Department of Electrical and Computer Engineering, University of Rochester, Rochester, NY, from 2010 to 2011. Henryk's research interests include image processing, human and computer vision and machine learning. Henryk is a recipient of several awards, including the Fellowship from the Minister of Higher Education of the Republic of Poland, the Polish Talents Award, the Crawford Prize for the best M. Sc. project and the 2014 SPIE Digital Photography X Best Paper Award.

Joyce Farrell is the Executive Director of the Stanford Center for Image Systems Engineering and a senior research associate in the Department of Electrical Engineering at Stanford University. She has a doctorate degree from Stanford University and more than 20 years of research and professional experience working at a variety of companies and institutions, including the NASA Ames Research Center, New York University, the Xerox Palo Alto Research Center, Hewlett Packard Laboratories and Shutterfly. She is also the CEO and founder of ImagEval Consulting, LLC.

Brian Wandell is the first Isaac and Madeline Stein Family Professor. He joined the Stanford Psychology faculty in 1979 and is a member, by courtesy, of Electrical Engineering and Ophthalmology. He is Director of Stanfords Center for Cognitive and Neurobiological Imaging, and Deputy Director of Stanfords Neuroscience Institute. Wandells research centers on vision science, spanning topics from visual disorders, reading development in children, to digital imaging devices and algorithms for both magnetic resonance imaging and digital imaging.

Brian Wandell graduated from the University of Michigan in 1973 with a B.S. in mathematics and psychology. In 1977, he earned a Ph.D. in social science from the University of California at Irvine. After a year as a postdoctoral fellow at the University of Pennsylvania, he joined the faculty of Stanford University in 1979.

In 1986, Wandell won the Troland Research Award from the National Academy of Sciences for his work in color vision. He was made a fellow of the Optical Society of America in 1990; in 1997 he became a McKnight Senior Investigator and received the Edridge Green Medal in Ophthalmology for work in visual neuroscience. In 2000, he was awarded the Macbeth Prize from the Inter-Society Color Council, and in 2007 he was named Electronic Imaging Scientist of the Year by the SPIE/IS&T, and he was awarded the Tillyer Prize from the Optical Society of America in 2008. He was elected to the American Academy of Arts and Sciences in 2011. Oberdorfer Award from the Association for Research in Vision and Ophthalmology, 2012. In 2014 he was awarded the highest honor of the Society for Imaging Science and Technology. Wandell was elected to the US National Academy of Sciences in 2003.